IOP Publishing Journal of Micromechanics and Microengineering

J. Micromech. Microeng. **17** (2007) 2006–2015 doi:10.1088/0960-1317/17/10/012

Surface roughness, asperity contact and gold RF MEMS switch behavior

O Rezvanian[1], M A Zikry[1], C Brown[2] and J Krim[2]

[1] Department of Mechanical and Aerospace Engineering, North Carolina State University, Raleigh, NC 26795, USA
[2] Department of Physics, North Carolina State University, Raleigh, NC 26795, USA

Received 7 May 2007, in final form 26 July 2007
Published 5 September 2007
Online at stacks.iop.org/JMM/17/2006

Abstract

Modeling predictions and experimental measurements were obtained to characterize the electro-mechanical response of radio frequency (RF) microelectromechanical (MEM) switches due to variations in surface roughness and finite asperity deformations. Three-dimensional surface roughness profiles were generated, based on a Weierstrass–Mandelbrot fractal representation, to match the measured roughness characteristics of contact bumps of manufactured RF MEMS switches. Contact asperity deformations due to applied contact pressures were then obtained by a creep constitutive formulation. The contact pressure is derived from the interrelated effects of roughness characteristics, material hardening and softening, temperature increases due to Joule heating and contact forces. This modeling framework was used to understand how contact resistance evolves due to changes in the real contact area, the number of asperities in contact, and the temperature and resistivity profiles at the contact points. The numerical predictions were qualitatively consistent with the experimental measurements and observations of how contact resistance evolves as a function of deformation time history. This study provides a framework that is based on integrated modeling and experimental measurements, which can be used in the design of reliable RF MEMS devices with extended life cycles.

(Some figures in this article are in colour only in the electronic version)

1. Introduction

Surface roughness and asperity behavior are critical factors that affect contact behavior at scales ranging from the nano to the micro in microelectromechanical, electronic and photonic devices. Specifically, in MEMS devices, large surface-to-volume ratios underscore that it is essential to understand and accurately predict how asperities behave in contact devices. MEMS switches, particularly those with radio frequency (RF) applications, have demonstrated significantly better performance over current electromechanical and solid-state technologies, which renders them as highly attractive alternatives for a variety of commercial and military applications [1–6].

One of the major objectives in the design of RF MEMS with metal contacts is to make repeatable and reliable electrical contacts. However, the complex physical interactions between thermo-mechanical deformation, current flow, and heating at the contact have made it extremely difficult to obtain accurate predictions of RF MEMS behavior, such that reliable devices can be designed for significantly improved life-cycles (see, for example, [7, 8]). Validated modeling methods can provide MEMS switch designers with insights on how the interrelated effects of the contact resistance, the surface roughness of the contact surfaces and the contact pressure evolve. Hence, guidelines can be incorporated in the design and fabrication process to effectively size critical components and forces to provide stable contact resistance for significantly improved device durability and performance.

Various analytical and numerical methods have been employed to study the contact mechanics of ideally smooth surfaces [9–14]. Since surface topographies are critical in MEMS devices, some probabilistic models have been proposed to account for asperity height variations (for

example, see [15, 16]). However, these studies do not account for the actual surface topographies related to the roughness of contact surfaces in MEMS devices. The random and multiscale nature of the surface roughness can be better described by fractal geometry [17–21]. The use of fractals to represent the surface roughness for contact analyses of MEMS devices has been used to relate contact parameters, such as the real area of contact, contact pressure and contact resistance [12, 20, 22–26].

However, what has been generally lacking is an integrated modeling framework that couples three-dimensional surface roughness representations with the thermo-mechanical deformation of surface asperities, and to relate these to device performance over time. Hence, in this study a three-dimensional fractal representation of surface roughness is used with a numerical framework to obtain predictions of thermo-mechanical asperity deformations of contacting surfaces as a function of time. Contact resistance behavior is then investigated and categorized for two surface roughness models with different roughness characteristics. Several resistance measures are then presented and their connection to other contact parameters, such as real contact area and the number of asperities in contact, is discussed. The resistivity of the contact material is assumed to vary by strain hardening, and also by softening effects due to Joule heating at the asperity micro-contacts. The contact material used in this investigation is gold, which is one of the widely used contact materials for low-current MEMS switches [27]. To validate our approach, we also compared our predicted results with a set of experiments that were undertaken to characterize the contact resistance of RF MEMS switches.

This paper is organized as follows. In section 2, the contact mechanics and topography of microscale contacts are presented. In section 3, the physics of contact resistance is discussed. The fabrication and experimental setup is presented in section 4. The fractal roughness models, the contact conditions and the numerical scheme are outlined in section 5. The results and discussion are given in section 6, followed by the summary and conclusions in section 7.

2. Contact mechanics and topography

Accurate modeling of the normal contact at the interface of the contact bump and the drain electrode in an RF MEMS switch requires the roughness profile of the two surfaces to be known. However, to simplify the contact problem, it can be assumed that the contact is between a rough and an infinitely smooth surface. This assumption is based on the fact that the drain electrode is generally significantly smoother than the contact bumps [20]. Furthermore, based on the composite theory of roughness, two rough surfaces in contact are equivalent to one infinitely smooth surface in contact with a rough surface, for which the composite roughness parameters are defined in terms of the roughness parameters of the original two surfaces.

Following the asperity-based model of Greenwood and Williamson [15], the asperities are dealt with individually. However, the deformation behavior of a contact asperity is influenced by other contact asperities, in that the share of the total applied load for each individual contact asperity will be determined by the set of all asperities that are in contact. In this study, the asperities are randomly distributed and the deformation of the asperities is obtained from the constitutive creep relations, and the contact areas are obtained from the deformed geometrical shapes of the contact asperities.

Fractal geometry can be used to obtain the random and multiscale topographies that pertain to most microscale engineering applications and devices [18–21]. Majumdar and Bhushan [25] used a fractal description of the surface topography in a contact problem to analyze the deformation behavior of the contacting asperities. Yan and Komvopoulos [26] used a three-dimensional fractal mechanics theory for elastic–plastic surfaces in normal contact, and they obtained numerical estimates for the average contact pressure and the real area of contact.

A realistic multi-scale three-dimensional fractal surface topography can be generated using a Weierstrass–Mandelbrot function [18, 21] and can be expressed as [26]

$$z(x, y) = L_0(G/L_0)^{D-2}(\ln(\gamma)/M)^{1/2} \sum_{m=1}^{M} \sum_{n=0}^{n_{\max}} \gamma^{(D-3)n} \times \{\cos\phi_{m,n} - \cos[(2\pi/L_0)\gamma^n(x^2+y^2)^{1/2} \times \cos(\tan^{-1}(y/x) - \pi\, m/M) + \phi_{m,n}]\}, \quad (1)$$

where L_0 is the sample length, G is the fractal roughness, which is a height scaling parameter independent of frequency, D is the fractal dimension ($2 < D < 3$), which its magnitude determines the contribution of high and low frequency components in the surface function z, γ is a scaling parameter, which is based on surface flatness and frequency distribution density, M is the number of superposed ridges used to construct the surface, $\phi_{m,n}$ is a random phase, n is a frequency index, where its maximum $n_{\max}$ is equal to int(Log(L_0/L_s)/Log(γ)) and L_s is a cut-off length.

During the first few contacts, the applied pressure is normally higher than the yield stress of the contact material. The initial contact pressure depends on the contact force and the size and the number of the asperities that are initially in contact. The contact force can be obtained from the electromechanical modeling of the cantilever beam, and the electrostatic field generated over the gate. During the period after the initial asperity deformation, contacting asperities are susceptible to creep under compressive strain. Creep deformation has been reported at micro-Newton level contact forces and low current levels ([27–29]). The rate of creep deformation is assumed to have a power-law dependence on the stress, and it can be stated as

$$\dot{\varepsilon} = A\sigma^p \exp\left(-\frac{Q_c}{kT}\right), \quad (2)$$

where $\dot{\varepsilon}$ is the strain-rate, A is a parameter relating to the material properties and the creep mechanism, σ is the stress, Q_c is the activation energy for creep, T is the absolute temperature and k is the Boltzmann constant ($k = 1.38 \times 10^{-23}$ J K^{-1}). The stress exponent p in (2) is usually between 3 and 10, and is determined by the material composition.

3. Physics of contact resistance and surface roughness

Due to the surface roughness, when two surfaces are in contact, the contact is made at a finite number of points, where the

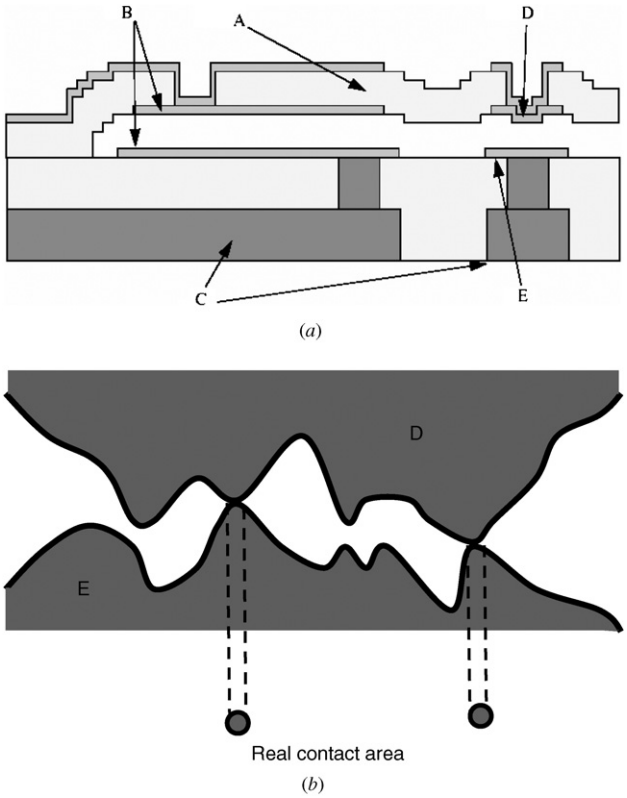

Figure 1. (*a*) Side view of an RF MEMS switch. A is the silica cantilever. B are gold actuation capacitors used to pull the cantilever downward to the contact bump D. When the contact bump and the gold contact on the signal line, E, are touching, the switch is closed and the signal can be transferred. C are copper transfer lines encapsulated in silica during the stack process. (*b*) Schematic of the surface asperities of the contact bump D and the gold contact E. Micro-contacts are established when the two surfaces touch.

asperities on both sides touch (figure 1(*b*)). These asperity contacts have different sizes, and since the electrical current is constricted to flow through these regions, it is essential to have an accurate representation of the contact area for predictions of the contact resistance. In addition to the role that the roughness has in limiting the contact area in the diffusive transport of electrons and increasing the regular ohmic resistance, for an asperity contact radius of the order of the electron mean free path, more electrons will be ballistically transported, and the contribution of the boundary scattering of electrons to the total constriction resistance can increase. Based on the range of the electron mean free path, which is approximately 50 nm in Au [30], and considering that MEMS contacts have been observed to have contact spots of the order of the electron mean free path [30], the boundary scattering effect can be critical for MEMS applications.

For a contact spot of radius a, and considering both ohmic and boundary scattering effects, the constriction resistance R_c can be given as [31, 32]

$$R_c = f\left(\frac{\lambda}{a}\right) R_M + R_S = f\left(\frac{\lambda}{a}\right)\frac{\rho}{2a} + \frac{4\rho\lambda}{3\pi a^2}, \tag{3}$$

where ρ is the electrical resistivity and λ is the electron mean free path. R_M denotes the Maxwell resistance, which is the resistance due to the lattice scattering mechanism [33], and R_S denotes the Sharvin resistance, which is due to the boundary scattering of electrons [34, 35]. In (3), $f(\lambda/a)$ is an interpolation function, which accounts for the transition between the two resistance regimes, and has the limiting values of 1 as the Knudsen numberλ/a approaches zero for $a \gg \lambda$, and 0.624 as λ/a approaches infinity for $a \ll l$. A commonly used expression for $f(\lambda/a)$ is [31, 32]

$$f\left(\frac{\lambda}{a}\right) = \frac{1 + 0.83(\lambda/a)}{1 + 1.33(\lambda/a)}. \tag{4}$$

To link the resistance of individual asperity contacts to the contact resistance, an effective contact resistance range has to be defined. In this study, we define a lower and an upper limit for the contact resistance. For the lower limit, it is assumed that contact spots do not interact with each other, and are in parallel. Hence, a lower limit for the effective contact resistance R_l can be approximated as

$$\frac{1}{R_l} = \sum_{i=1}^{N} \frac{1}{R_{ci}}, \tag{5}$$

where N is the number of asperity contacts and R_{ci} is the resistance of contact spot i. An upper limit for the effective contact resistance can be obtained by replacing all asperity contacts with a single asperity with a contact area equal to the total contact area of all the individual asperity contacts with an effective radius a_{eff} and an average resistivity ρ_{av}. Using (2), the upper limit for the contact resistanceR_u is

$$R_u = f\frac{\rho_{av}}{2a_{\text{eff}}} + \frac{4\rho_{av}\lambda}{3\pi a_{\text{eff}}^2}. \tag{6}$$

Inelastic deformations result in the hardening of the contact material, which, in turn, increases the resistivity. On the other hand, as the contact asperities become extensively deformed, the contact area increases. Hence, there are two competing events in which the net effect will be highly dependent on the roughness characteristics. These interactions are further exacerbated by the increases in the contact temperature due to Joule heating. In addition to the direct contact heating effects on resistivity, if the temperature becomes high enough, the contact material can soften [30, 33], countering the hardening effects of inelastic deformations. At the same time, increases in temperature can also accelerate the material's creep response over a rather long period of time, which can subsequently lead to device failure.

In the present model, strain-hardening and softening effects on resistivity are accounted for through a power-law formulation [36] as

$$\rho = \bar{\rho}\left(1 + \frac{\varepsilon_p}{\varepsilon_{\text{ref}}}\right)^q \left(1 - \exp\left(-\frac{Q}{kT_c}\right)\right), \tag{7}$$

where $\bar{\rho}$ is the average resistivity of a contact spot at temperature T_c, ε_p is the plastic strain, ε_{ref} is a reference strain, q is a material dependent parameter, Q is the activation energy for the mechanism by which stored dislocations are recovered or annihilated and k is Boltzmann's constant.

Using the basic definitions of the Joule heating and the heat flow, some contact heating models relate the contact spot temperature T_c, controlled by the joule heating mechanism, to the contact voltage V_c, without considering the size effects of the asperities in contact [8, 33, 37]. With the size of the contact spots being close to the electron mean free path of the

contact material [30], the boundary scattering contribution to the contact resistance increases. However, boundary scattering does not result in the Joule heating of the contact spots [38]. Hence, following the asperity-heating model of [30], contact spot temperature can be stated as

$$T_c = \sqrt{\frac{\gamma R_M}{4LR_c} V_c^2 + T_0^2}, \tag{8}$$

where L is the Lorenz number ($L = 2.45 \times 10^{-8}$ W Ω K^{-2}) and T_0 is the ambient temperature.

4. RF MEMS fabrication and experimental setup

A number of experiments were carried out at the Nanoscale Tribology Laboratory at North Carolina State University, with the goal that a comparison can be made between the experimental and numerical modeling results. The RF MEMS devices used for these experiments are commercially available single pole double throw switches by wiSpry Inc. Each die contains four double throw pairs. The switch consists of a cantilever arm with a pair of gold contacting dimples at the termination (figure 1(*a*)). The switches are fabricated using the wiSpry metal surface micromachining process. The die substrate is a silicon wafer. Gold and copper transfer lines are interlaced with silicon and oxide layers during the stack process. Sacrificial layers are subsequently etched away creating the three-dimensional cantilever structure and exposing the electrode plates used for actuation and the contact dimples which transfer the input signal. An electrostatic force is used to pull the cantilever arm down forcing the upper contacts dimples with the lower electrodes. The beam length is 135.5 μm with a width of 251 μm. The contact bumps are 6 μm in diameter and are separated by 55 μm. The travel distance of closure is 2 μm.

The devices are mounted on gold sidebrazed ceramic packages with 1 mil (25 μm) gold wirebonds connecting the device to the package, and the package is mounted inside of a vacuum system. The vacuum system is pumped to 1–5 mTorr., and then backfilled with helium. The helium pressure was held at 760 Torr. and at 293 K. This helium environment was also used to control stiction events. The vacuum environment created before backfilling the helium sufficiently removes moisture; however, a thin layer of hydrocarbon is most likely present during testing. Two Keithley 2400 source-meters were used to actuate the switch and to record the resistance across the contacts using the four-point probe technique. Varying the output voltage from the source-meter changes the contact force. For the test device, 33 V generated a stable contact resistance for testing. Both source meters were controlled using LabVIEW software. Before each test, the switch was cold-switched 250 times. After this, the switch remained in the closed position, and a current of 100 μA was applied. A resistance measurement was taken from only one switch on the double throw, once per second for the duration of the testing period.

5. Contact models

Two surface roughness models were obtained using (1), over an area of 4 × 4 microns, which is close to the area of the contact

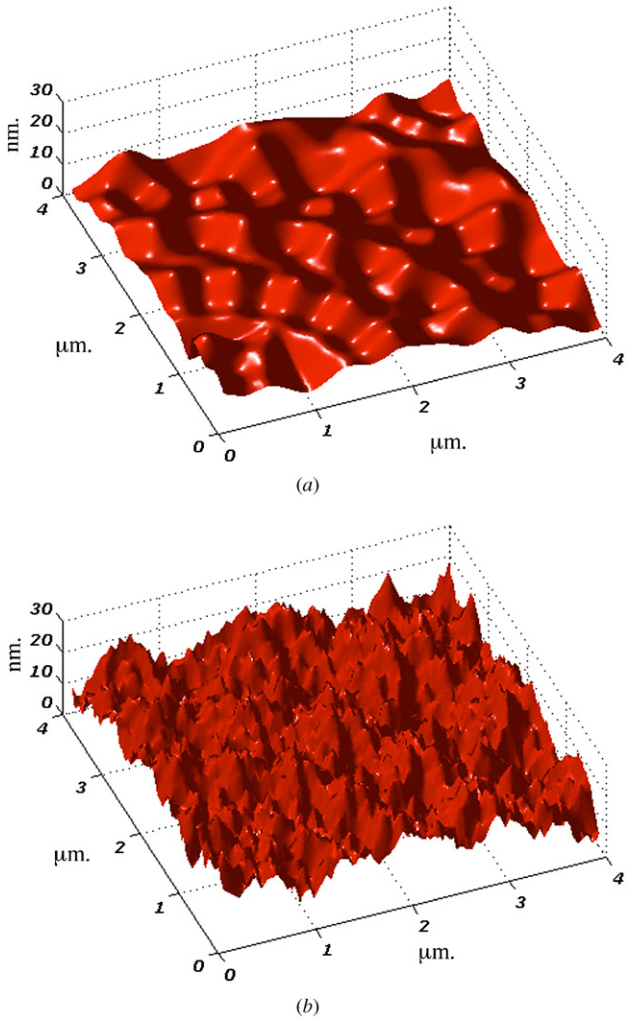

Figure 2. Three-dimensional fractal surface topographies generated using a Weierstrass–Mandelbrot function: (*a*) model 1 has a peak-to-valley of 12.8 nm and an RMS of 7.2 nm; (*b*) model 2 has a peak-to-valley of 27.1 nm and an RMS of 14.9 nm.

bumps in our fabricated RF MEMS switches. The topography was varied, so that we can understand how roughness can affect contact behavior. In model 1 (figure 2(*a*)) a surface roughness profile with a peak-to-valley of 12.8 nm and an RMS of 7.2 nm was generated. Model 2 (figure 2(*b*)) has a peak-to-valley of 27.1 nm and an RMS of 14.9 nm. These values are representative of roughness profiles for gold RF MEMS switches. The mating surface is assumed to be flat and infinitely smooth. The parameters used in (1) for each model are given in table 1. As noted earlier, the contact material is gold, and its electro-mechanical properties are given in table 2. For the current model, it is assumed that the ambient temperature is 293 K.

Contact forces in MEMS switches are typically in the range of a few μNs to as high as about 1 mN [27]. In this model, the applied contact force was chosen to be 50 μN, pertaining to a gold cantilever beam with dimensions of 150 × 250 × 0.5 μm, and a gap of 2 μm. The switch is assumed to remain in the closed position for the duration of the simulation, and it is also assumed that there is no insulating film effect. This is done so that we can better understand the direct effects

Table 1. Roughness parameters.

Parameter	Unit	Model 1	Model 2
L	m	4×10^{-06}	4×10^{-06}
G	m	0.5×10^{-11}	9.5×10^{-11}
D	–	2.5	2.6
γ	–	1.5	1.5
M	–	10	10
L_s	m	600×10^{-09}	3×10^{-09}

Table 2. Electromechanical properties of gold.

Electrical resistivity, ρ	2.5×10^{-08} Ω m
Power exponent in (2), p	7
Coefficient in (2), A	9×10^{-16}
Activation energy in (2), Q_c	3×10^{-19} J
Reference strain in (7), ε_{ref}	0.001
Power exponent in (7), q	0.1

of surface roughness on the electro-mechanical behavior of RF MEMS switches with normal contact. Also the current model does not account for the generated debris from the fracture and crushing of the contact asperities, which is known to influence the electro-mechanical response of the RF MEMS switches [39].

In RF MEMS switches with normal contact, the lateral deformations of asperities can be assumed to be negligible. Since creep is a long-term deformation mechanism, the normal finite deformations of contact asperities can then be obtained by a power-law constitutive relation (equation (2)). Since the generated surface roughness models do not necessarily have any prescribed asperity geometries, a numerical scheme has to be used to generate asperity geometries, which instead of having smooth surfaces (S1 in figure 3(*a*)) have irregular surfaces (S2 in figure 3(*a*)). A grid of x and y coordinates has been used to take sampling points on the surface of the asperities. The asperity geometries are obtained by connecting these sampling points. S2 approaches S1 when the number of sampling points increases (figure 3(*a*)). In this scheme, asperities can have any arbitrary geometry. The asperity geometries are constructed from layers that stack upon each other in the z direction (figures 3(*b*), (*c*)). The cross sectional area of each layer is assumed to be constant along its thickness, and is determined by using the x and y coordinates of the sampling points, which define that layer (figure 3(*c*)). The thickness of each layer is obtained by the z coordinates of the sampling points. The stresses and strains for each individual asperity in contact are then obtained for each individual layer, and the far-field approach is determined from the collective creep response of the contact asperities. The asperity tips that establish contact are identified at each time step by comparing the far-field approach with the asperity heights. An 80 by 80 grid of x and y coordinates is used to obtain the updated contact areas. Consequently the contact pressure, the resistance, the temperature and the material properties are updated at each time step. Based on the deformations induced by the contact and asperity interactions, the number of asperities in contact and an effective radius for the contact area of each individual asperity are determined at each increment. Since the asperity contact layers are not necessarily circular, as an approximation the contact radius used in equation (3) is taken as the radius of

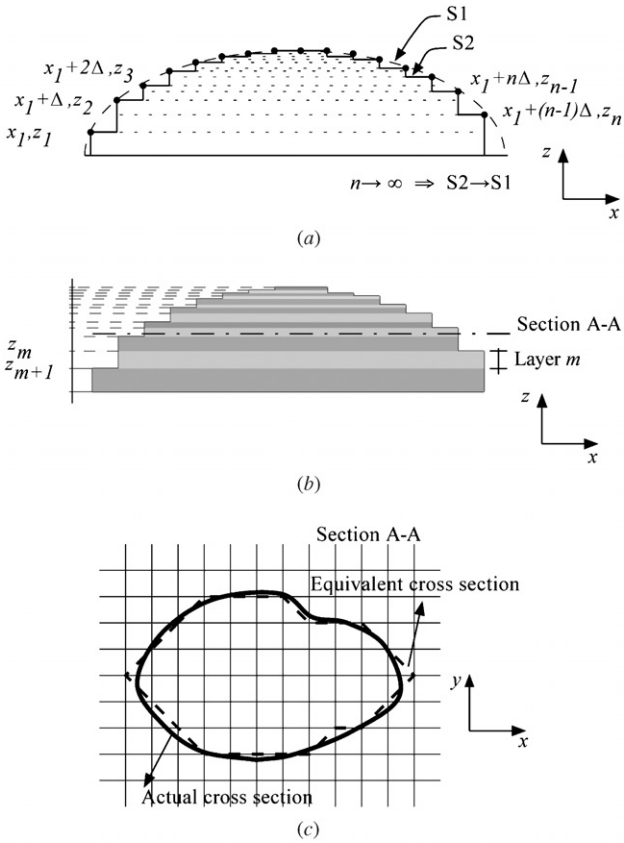

Figure 3. (*a*) Schematic front view of a cross section of the actual asperity geometry with a smooth surface (S1), and its equivalent geometry with an irregular surface (S2) that is obtained by connecting the sampling points. (*b*) The asperity geometry that is assumed as stacked layers with uniform cross sectional areas along the thickness direction. (*c*) A schematic top view of a cross section of the actual asperity, and its equivalent geometry that is obtained by connecting the corresponding sampling points.

a circle of equal area (see figure 3(*c*)). It is also assumed that the thermal boundary conditions are fixed.

6. Results and discussion

The ratio of the real contact area to the total area for the two roughness models is shown in figure 4. It is seen that the contact area increases with a steep slope at the beginning, which is due to the initial high applied pressure. The high applied pressure results in large deformations in the contact asperities. The asperity deformations, in turn, lower the applied pressure in two different ways. Firstly, as the asperities deform, more asperities come into contact. Secondly, the cross sectional area of asperities generally increases as they are pressed down. Hence, the real contact area increases. The decreased applied pressure, then, along with the strain hardening of the material, reduces the rate of increase of the contact area. It is also seen from figure 4 that after 48 h the real contact areas are almost equal, and they are approximately 7% of the apparent area for both roughness models. As noted earlier, roughness parameters have been selected in such a way that generate approximately equal real contact areas for the two models, but with different number of contact asperities. The

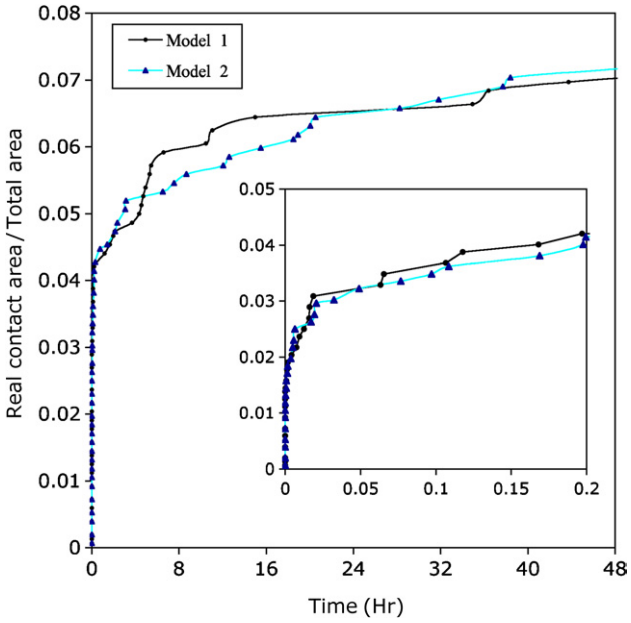

Figure 4. Ratio of the real contact area to the apparent area over a 48 h time span for the two surface roughness models. The inset magnifies the initial 12 min.

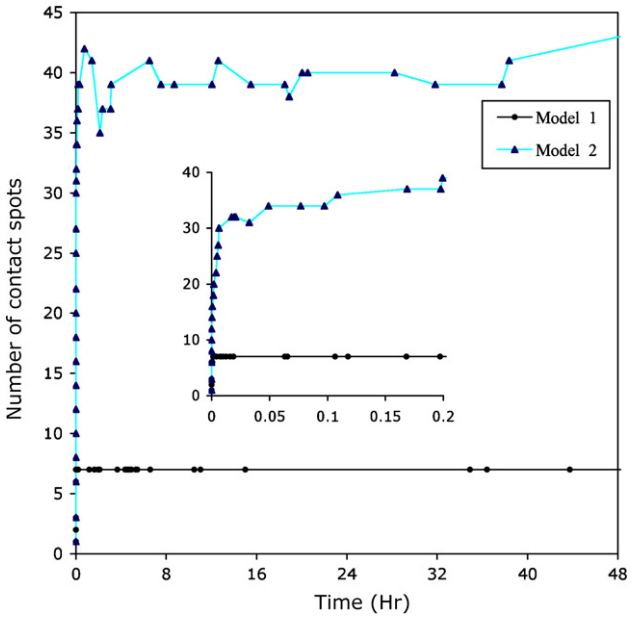

Figure 5. Number of the contact spots over a 48 h time span for the two surface roughness models. The inset magnifies the initial 12 min.

number of micro-contact spots for the two roughness models is shown in figure 5. Model 1 has very few asperities in contact, with their number being almost constant over the contact period. In contrast, model 2 has considerably more asperities in contact with their numbers increasing initially, and then fluctuating over time. The number of micro-contacts decreases when some micro-contacts coalesce, and it increases when new micro-contacts are established. The coalescence and generation of micro-contacts changes the constriction resistance, which is also affected by how the micro-contacts

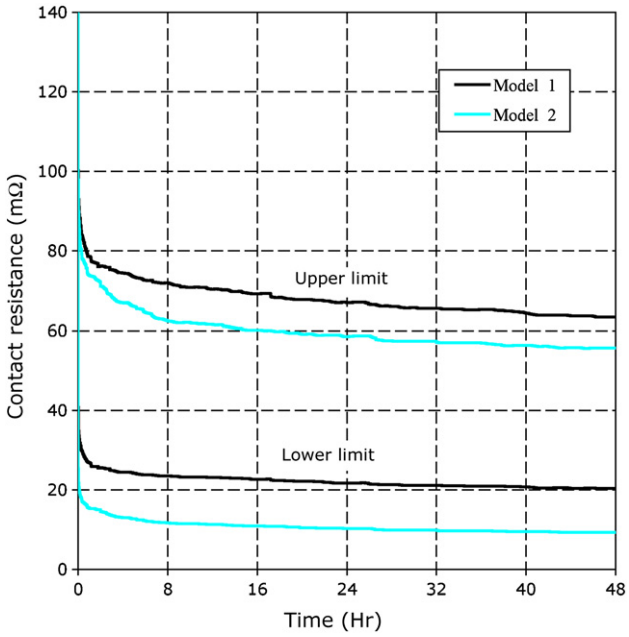

Figure 6. The lower and upper limits of the contact resistance over a 48 h time span for the two surface roughness models.

are distributed over the apparent area. Based on this, two limit cases can be considered for how the micro-contacts are distributed, and accordingly two limits can be determined for the contact resistance.

For the two roughness models, the lower and upper limits of contact resistance have been calculated over time, and the results are shown in figure 6. The lower limit corresponds to the case for which each micro-contact is assumed to be far enough from the others so that there will be no neighboring asperity effects. The upper limit corresponds to the case for which a large micro-contact is assumed to form by the coalescence of all the micro-contacts. Two stages of decrease can be seen in the curves of figure 6. The contact resistance initially decreases sharply until it reaches a rather stable level, during which the contact resistance continues to gradually decrease. The initial rate of reduction of contact resistance is associated with the initial deformation rate of asperities. Consequently, the increased contact area and the number of contact spots reduces the applied pressure, which in turn decreases the deformation rate of asperities. The results show that for the selected roughness parameters for both roughness models, the overall effect of increased resistivity at the asperity contacts due to the strain hardening is dominated by the contact area effect. Model 1 has an initial lower limit contact resistance of 44 m Ω, and an upper limit of about 125 m Ω. After the initial deformation of the asperities for 10 min, the contact resistance decreases to between 32 and 88 m Ω. After 48 h, the contact resistance reduces to between 20 and 63 m Ω, which on average is about 47% of the initial value (figure 6). Model 2 has an initial contact resistance between 40 and 127 m Ω, which after 10 min decreases to between 20 and 84 m Ω. The contact resistance level after 48 h falls between 11 and 57 m Ω, which on average is about 37% of the initial value (figure 6). After 48 h, the contact resistance in model 1, which almost has the same contact areas, is 1.22 times higher than the

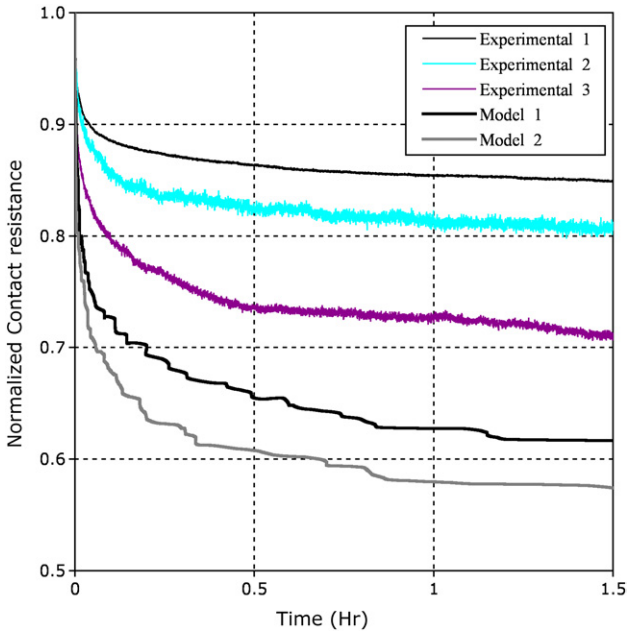

Figure 7. Normalized contact resistance over a 90 min time span.

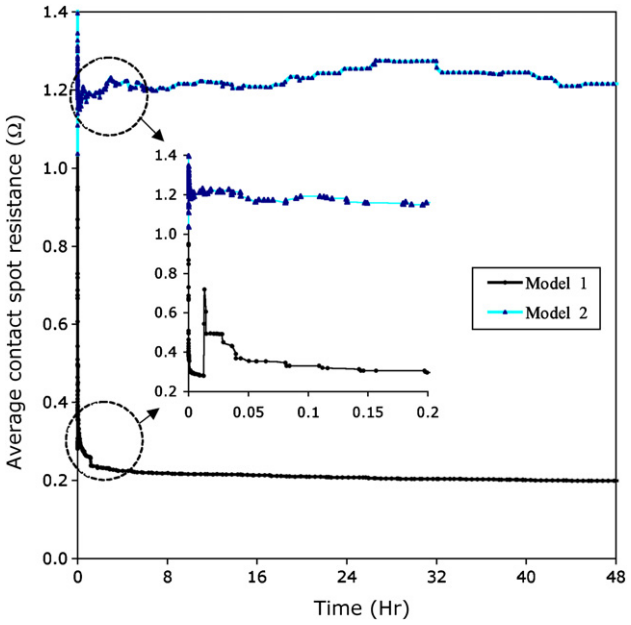

Figure 8. Average contact spot resistance of the two surface roughness models over a 48 h time span. The inset magnifies the initial 12 min.

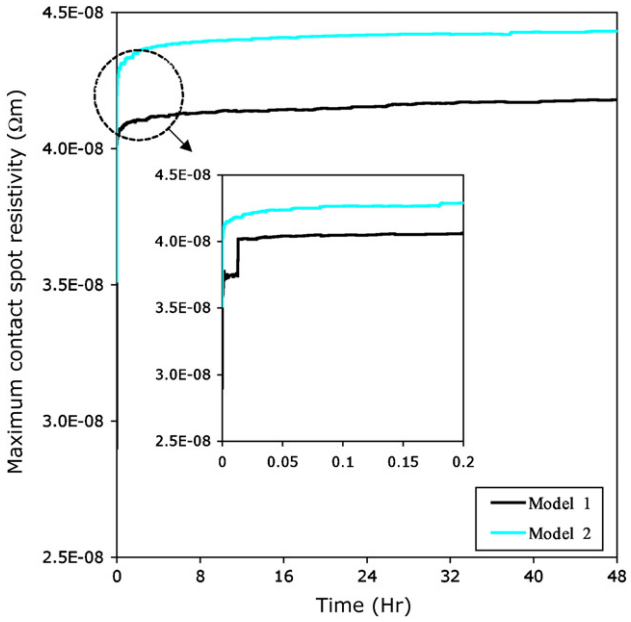

Figure 9. Maximum resistivity at the contact spots for the two surface roughness models over a 48 h time span. The inset magnifies the initial 12 min.

contact resistance of model 2; the difference can be attributed to the number of the micro-contacts in each model. Reported minimum contact resistance, in previous studies, varies from less than 0.1 Ω to several ohms at loads from 25 μN to 300 μN for gold-on-gold contacts in different environments [27]. Majumdar *et al* [20] reported a contact resistance between 60 and 130 m Ω for a population of 50 asperities, and a contact resistance between 80 and 110 m Ω for a population of five asperities, both pressed by a 50 μN contact force. Hence, it is seen that the predicted contact resistance values for the two roughness profiles of this study are within the same range of these cited studies.

To further validate our model, we also compared the predicted contact resistance of the roughness models with experimental measurements described in section 4. Three experimentally measured contact resistance curves over a 90 min time span are shown in figure 7, along with the predicted upper limits of the contact resistance for the two roughness models. To be able to make a meaningful comparison, each data set is normalized by its respective maximum value. The experimental and the predicted results show a similar evolution for the contact resistance. Quantitatively, however, the experimental measurements show a less resistance drop over the time. On average, the experimental measurements show that the contact resistance drops to about 80% of its initial maximum value after 90 min, while the simulations predict a 40% drop (60% of their initial value).

Another resistance measure that can be used to better understand the effects of roughness characteristics on the total resistance response of a population of micro-contacts is the average resistance of the individual contact asperities (figure 8). By comparing figures 6 and 8, it can be seen that the estimated upper limit for the contact resistance, when stabilized, is significantly lower than the average resistance of the individual contact spots. The average resistance of the individual micro-contacts of model 2 initially increases to about 1.4 Ω, and then fluctuates around 1.2 Ω. The initial increase is due to strain hardening and increased resistivity, which locally surmounts the contact area effects.

In contrast, the average resistance of the micro-contacts in model 1 is initially about 1.15 Ω, which falls down to between 0.2 and 0.3 Ω, then increases and falls down again. The fluctuations best show how strain hardening and increased resistivity compete with contact area effects. Figure 9 then shows to what extent the strain hardening can increase the resistivity of the contact material. It is seen from the curves of

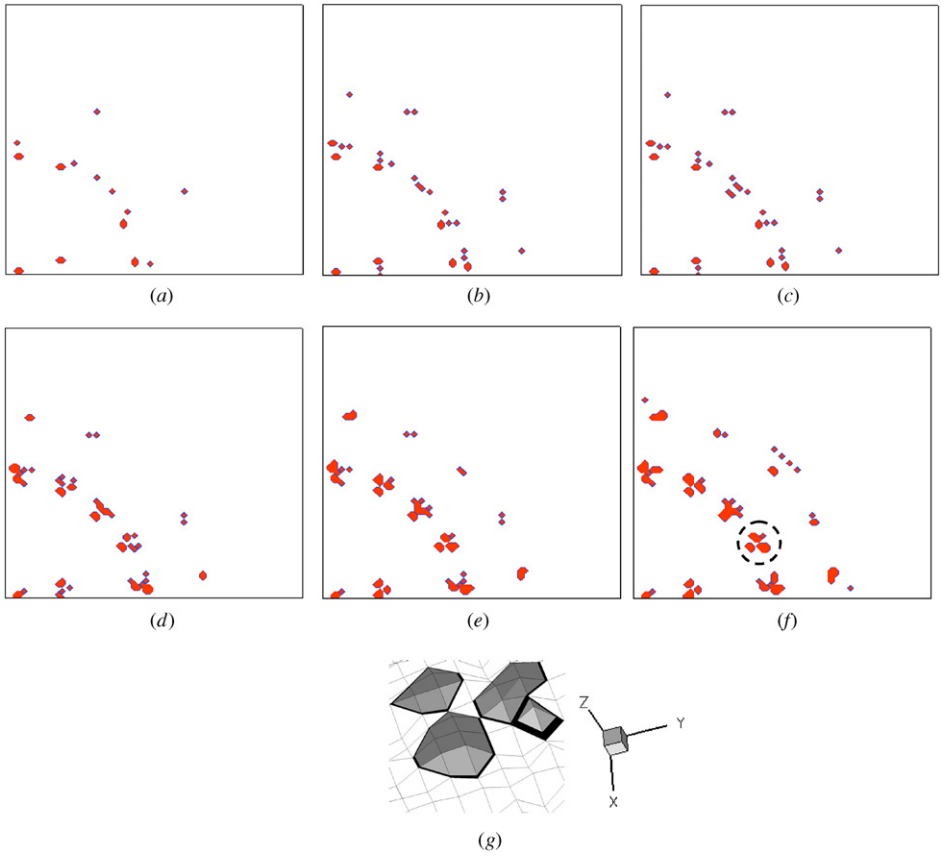

Figure 10. Top-view snap shots of the contact evolution for model 2: (*a*) after 1 s, the real contact area is 1.31%, the contact resistance is 27 ∼ 77 m Ω and the applied pressure is 237 Mpa; (*b*) after 30 s, the real contact area is 2.50%, the contact resistance is 14 ∼ 56 m Ω and the applied pressure is 125 MPa; (*c*) after 1 min, the real contact area is 2.63%, the contact resistance is 14 ∼ 55 m Ω and the applied pressure is 119 Mpa; (*d*) after 1 h, the real contact area is 4.47%, the contact resistance is 9 ∼ 42 m Ω and applied pressure is 70 Mpa; (*e*) after 10 h, the real contact area is 5.60%, the contact resistance is 8 ∼ 37 m Ω and the applied pressure is 56 Mpa; (*f*) after 40 h, the real contact area is 7.0%, the contact resistance is 7 ∼ 34 m Ω and the applied pressure is 44 Mpa; (*g*) magnified 3D view of the asperity cluster circled in (*f*).

figure 9 that in model 1 the maximum resistivity increases to about 4.1×10^{-08} Ω m at deformed asperity contacts, which is 1.64 times the initial resistivity. In model 2, the maximum resistivity reaches to about 4.4×10^{-08} Ω m, which is 1.76 times the initial resistivity. Higher resistivity in model 2 is an indication of asperities with higher curvatures, which can also be seen in figure 2.

Top-view snap shots of contact evolution over the 48 h time span for model 2 are also shown in figure 10. The snap shots show how micro-contacts are distributed and clustered over the apparent contact area. The contact area, resistance and applied pressure are also given for each snapshot.

The temperature increase at contact spots is insignificant in both models for the voltage drop of 1 mV. However, for a voltage drop of 0.1 V, a very high current flows through the micro-contacts, which results in temperatures of up to 370 K at the contact spots. The current contour for a 1 mV voltage drop applied to model 2 is shown in figure 11. The 3D contour shows that, after 48 h, the current flow has increased to about 7 mA at some contact spots, which is within the reported range for gold contacts [27]. Furthermore, the maximum allowable current for gold contacts has been reported to be from 20 to 500 mA in different environments [27].

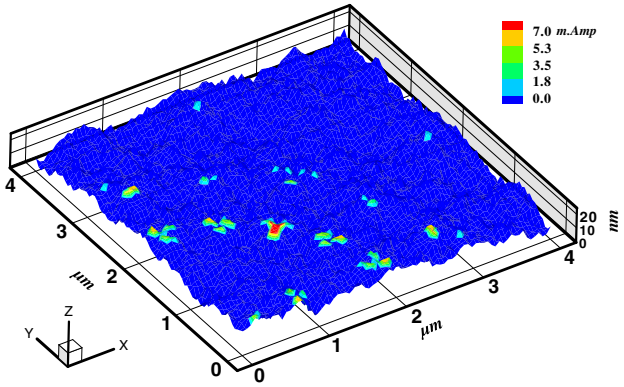

Figure 11. Contour of current for a voltage drop of 1 mV.

7. Conclusions

Modeling predictions and experimental measurements were obtained to characterize the electro-mechanical response of RF MEMS switches due to variations in surface roughness and finite asperity deformations. Three-dimensional surface roughness profiles were generated, based on a Weierstrass–

Mandelbrot fractal representation, to match the measured roughness characteristics of contact bumps of manufactured RF MEMS switches. Real areas of contact and the number of contact asperities were then obtained over the time, as a function of the asperity deformations under applied pressure.

The interrelated effects of roughness characteristics, material hardening due to creep deformation, and softening due to temperature increases from Joule heating were investigated on contact resistance. Changes in the constriction resistance of individual asperities were shown to depend on the two competing events of increases in the contact area and the electrical resistivity. The numerical predictions and the experimental measurements indicate that there are two main stages related to the variation of the contact resistance. An initial decrease with a steep slope, with a subsequent gradual decrease was characteristic of the contact resistance behavior. In the initial stage, the decrease is attributed to the high applied pressure, and the slightly strain-hardened contact material. In the second stage, the applied pressure had considerably decreased, and the contact material had extensively strain hardened.

The results indicate that a very small percentage of the apparent contact area, in both cases less than 10%, conducts the electrical current. They also indicate that asperity coalescence prevents the unlimited increase of the number of the micro-contacts. Furthermore, based on the distribution, size and number of the micro-contacts, the results indicate that the electrical interactions of the neighboring micro-contacts cannot be neglected in the design of RF MEMS devices. The results also show different characteristic contact resistance behaviors for a population of asperities versus individual asperities. This modeling approach, in conjunction with the experimental measurements and observations, can be used as a framework to design reliable RF MEMS devices with extended lifetimes.

Acknowledgments

The authors gratefully acknowledge useful support and interactions with Art Morris of WiSpry, Inc. This work was funded by the AFOSR Extreme Friction MURI program, AFOSR grant FA9550-04-1-0381.

References

[1] Barker N S and Rebeiz G M 1998 Distributed MEMS true-time delay phase shifters and wide-band switches *IEEE Trans. Microw. Theory Tech.* **46** 1881–90
[2] Brown E R 1998 RF-MEMS switches for reconfigurable integrated circuits *IEEE Trans. Microw. Theory Tech.* **46** 1868–80
[3] Hah D, Yoon E and Hong S 2000 A low-voltage actuated micromachined microwave switch using torsion springs and leverage *IEEE Trans. Microw. Theory Tech.* **48** 2540–5
[4] Park J Y, Kim G H, Chung K W and Bu J U 2001 Monolithically integrated micromachined RF MEMS capacitive switches *Sensors Actuators* A **89** 88–94
[5] Taylor W P, Brand O and Allen M G 1998 Fully integrated magnetically actuated micromechanical relays *J. Microelectromech. Syst.* **7** 181–91
[6] Yao Z J, Chen S, Estelman S, Denniston D and Goldsmith C 1999 Micromachined low-loss microwave switches *J. Microelectromech. Syst.* **8** 129–134
[7] Rebeiz G M 2003 *RF MEMS, Theory, Design, and Technology* (New York: Wiley)
[8] Hyman D and Mehregany M 1999 Contact physics of gold microcontacts for MEMS switches *IEEE Trans. Compon. Packag. Technol.* **22** 357–64
[9] Johnson K L 1985 *Contact Mechanics* (Cambridge: Cambridge University Press)
[10] Kennedy F E and Ling F F 1974 Elasto-plastic indentation of a layered medium *J. Eng. Mater. Technol.* **96** 97–103
[11] Komvopoulos K 1988 Finite element analysis of a layered elastic solid in normal contact with a rigid surface *J. Tribol.* **110** 477–85
[12] Komvopoulos K and Ye N 2001 Three-dimensional contact analysis of elastic-plastic layered media with fractal surface topographies *J. Tribol.* **123** 632–40
[13] Kral E R and Komvopoulos K 1996 Three-dimensional finite element analysis of surface deformation and stresses in an elastic-plastic layered medium subjected to indentation and sliding contact loading *J. Appl. Mech.* **63** 365–75
[14] Mesarovic S Dj and Fleck N A 1999 Spherical indentation of elastic-plastic solids *Proc. R. Soc. London* A **455** 2707–28
[15] Greenwood J A and Williamson J B P 1966 Contact of nominally flat surfaces *Proc. R. Soc. London* A **295** 300–19
[16] Larsson J, Biwa S and Storakers B 1999 Inelastic flattening of rough surfaces *Mech. Mater.* **31** 29–41
[17] Berry M V and Lewis Z V 1980 On the Weierstrass–Mandelbrot fractal function *Proc. R. Soc. London* A **370** 459–84
[18] Borodich F M and Onishchenko D A 1999 Similarity and fractality in the modeling of roughness by a multilevel profile with hierarchical structure *Int. J. Solids Struct.* **36** 2585–12
[19] Majumdar A and Tien C L 1990 Fractal characterization and simulation of rough surfaces *Wear* **136** 313–27
[20] Majumdar S, McGruer N E, Adams G G, Zavracky P M, Morrison R H and Krim J 2001 Study of contacts in an electrostatically actuated microswitch *Sensors Actuators* A **93** 19–26
[21] Mandelbrot B B 1983 *The Fractal Geometry of Nature* (New York: Freeman)
[22] Blackmore D and Zhou J G 1998 Fractal analysis of height distributions of anisotropic rough surfaces *Fractals* **6** 43–58
[23] Ciavarella M, Demelio G, Barber J R and Jang Y H 2000 Linear elastic contact of Weierstrass profile *Proc. R. Soc. London* A **456** 387–405
[24] Komvopoulos K 2000 Head-disk interface contact mechanics for ultra-high density magnetic recording *Wear* **238** 1–11
[25] Majumdar A and Bhushan B 1991 Fractal model of elastic-plastic contact between rough surfaces *J. Tribol.* **113** 1–11
[26] Yan W and Komvopoulos K 1998 Contact analysis of elastic-plastic fractal surfaces *J. Appl. Phys.* **84** 3617–24
[27] Patton S T and Zabinski J S 2005 Fundamental studies of Au contacts in MEMS RF switches *Tribol. Lett.* **18** 215–30
[28] Budakian R and Putterman S J 2002 Time scales for cold welding and the origins of stick-slip friction *Phys. Rev.* B **65** 235429
[29] Gregori G and Clarke D R 2006 The interrelation between adhesion, contact creep, and roughness on the life of gold contacts in radio-frequency microswitches *J. Appl. Phys.* **100** 094904–1
[30] Jensen B D, Chow L L, Huang K, Saitou K, Volakis J L and Kurabayashi K 2005 Effect of nanoscale heating on electrical transport in RF MEMS switch contacts *J. Microelectromech. Syst.* **14** 935–46
[31] Wexler G 1966 The size effect and the non-local Boltzmann transport equation in orifice and disk geometry *Proc. Phys. Soc.* **89** 927–41

[32] Nikolic B and Allen P B 1999 Electron transport through a circular constriction *Phys. Rev.* B **60** 3963–9
[33] Holm R 1967 *Electric Contacts: Theory and Applications* 4th edn (Berlin: Springer)
[34] Jansen A G M, van Gelder A P and Wyder P 1980 Point-contact spectroscopy in metals *J. Phys. C: Solid State Phys.* **13** 6073–118
[35] Sharvin Y V 1965 A possible method for studying Fermi surfaces *J. Exp. Theor. Sci.* **21** 655–6
[36] Zikry M A 1994 An accurate and stable algorithm for high strain-rate finite strain plasticity *Comput. Struct.* **50** 337–50
[37] Yan X, McGruer N E, Adams G G and Majumdar S 2003 Finite element analysis of the thermal characteristics of MEMS switches *Proc. 12th Int. Conf. on Transducers, Solid-State Sensors, Actuators and Microsystems*
[38] Weber L, Lehr M and Gmelin E 1996 Investigation of the transport properties of gold point contacts *Physica* B **217** 181–92
[39] Alsem D H, Stach E A, Dugger M T, Enachescu M and Ritchie R O 2007 An electron microscopy study of wear in polysilicon microeletromechanical systems in ambient air *Thin Solid Films* **515** 3259–66